• Supplementary File •

A Reconfigurable 8×8SPAD Array LiDAR Receiver with On-chip Noise Suppression and Reflectivity Compensation for High-Frame-Rate Applications

Zichen Wei[1], Dongsheng Liu[2] & Yu Yu[1]*

[1]*Wuhan National Laboratory of Optoelectronics, Huazhong University of Science and Technology, Wuhan 430074, China;*
[2]*School of Integrated Circuits, Huazhong University of Science and Technology, Wuhan 430074, China*

Appendix A The 8×8 SPAD Receiver Array

Fig. A1 illustrates the detailed circuit of the proposed 8 × 8 SPAD receiver array. Each SPAD is paired with an active quenching and reset circuit to minimize deadtime. Each SPAD's quenching and reset circuit is independently controlled by an enable signal, SPAD_EN, and outputs through a dedicated signal, SPAD_OUT. These output signals are combined through an OR gate to generate the STOP signal.

Specifically, in Fig. A1, M1 and M2 serve as fast quenching resistors, while M5 and M6 are thick-gate MOSFETs designed to prevent breakdown and convert the SPAD anode voltage to digital pulses. The delay circuit is composed of multiple inverters, ultimately achieving phase inversion. After 10 nanosecond delay, the output pulse activates M3 to reset the SPAD, and M4 is used to disable the SPAD via the enable signal SPAD_EN.
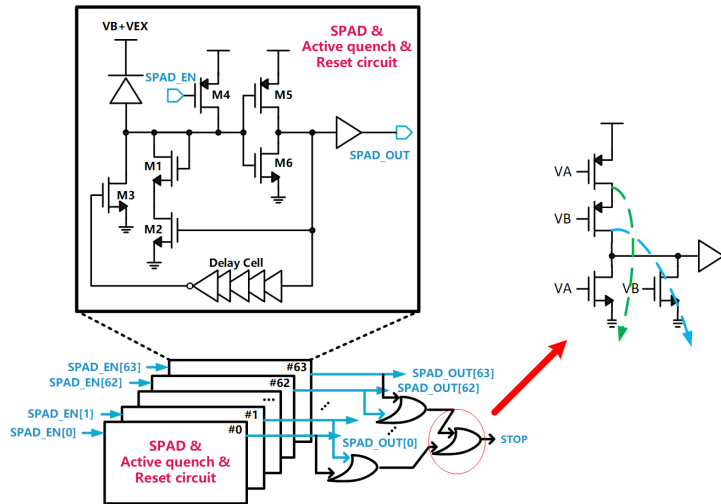

Figure A1   The diagram of the proposed 8×8 SPAD receiver array.

An OR gate effectively merges multiple trigger signals into a single trigger signal. However, merging 64 trigger signals requires at least six OR gates, which introduces significant nonlinearity. As shown in Fig. A1, when VA toggles, the signal propagates through the path indicated by the blue dashed line, discharging the OR gate's output charge from VDD to GND. Similarly, when VB toggles, the signal discharges through the green path. However, if two signals arrive simultaneously, the charge is discharged through both the blue and green paths simultaneously, resulting in a faster toggle time compared to a single discharge event.

Simulations show that each OR gate introduces approximately 50 ps of delay variation. However, due to the inherent jitter in SPAD triggering times, the actual error in real-world conditions is larger than the simulation results. Moreover, SPADs exhibit significant delay variations under weak and strong echo conditions, leading to noticeable discrepancies. As a result, during actual measurements, objects with high and low reflectivity can cause range measurement errors exceeding 60 cm.

* Corresponding author (email: yuyu@mail.hust.edu.cn)

The independent enable signal, SPAD_EN, for each SPAD allows dynamic control, enabling or disabling individual SPADs within the array. This configurability means that the active SPAD region can be reconfigured to match the laser focal point. As illustrated in Fig. A2, the lens focuses the returning light pulses at the focal point, triggering only the SPADs within this region, while SPADs outside the focal area remain unaffected by the laser and respond only to background noise. For example, while the total SPAD array area is $600 \times 600 \ \mu m^2$, the laser focal point occupies approximately $200 \times 200 \ \mu m^2$. After directing the light towards a target at a specific distance, each SPAD is sequentially enabled to determine whether the corresponding echo falls within its sensitive area (a TDC result is generated if the light echo is detected by a specific SPAD). Subsequently, each SPAD is enabled individually to assess the location where the echo is focused. This approach allows for the differentiation between SPADs located within the focal point and those situated outside of it. SPADs outside the focal point are deactivated, which minimizes background noise interference. During module assembly, the SPAD_EN signals need to be sequentially activated while facing the target to determine the position where the reflected light is focused.
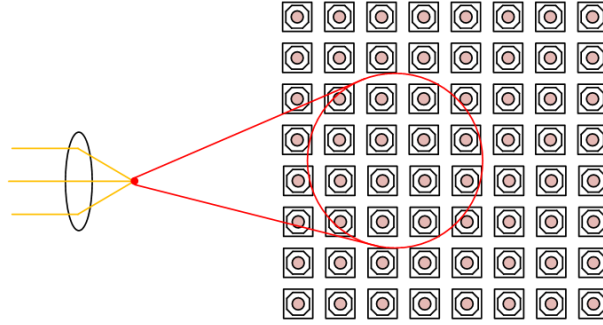

Figure A2   Laser Foal Point.

Additionally, the independent output signal, SPAD_OUT, from each SPAD is aggregated to determine the total number of triggered SPADs. This count reflects the laser intensity and serves as a basis for compensating walk error as well as photon coincidence detection for background inference mitigation.

Appendix B   Multi-echo TDC with Pulse Intensity Capture Capability

This paper proposes a Multi-echo TDC with Pulse Intensity Capture Capability, which features a high time resolution of 31.25 ps. It can record multiple echoes while simultaneously capturing the number of SPAD triggers. This information is further utilized for intensity recording in the histogram module and photon correlation detection. Fig. B1 and Fig. B2 illustrate the block diagram and signal timing diagram of the DLL and TDC circuits, respectively. Operating at 500 MHz, the coarse counter and DLL generate the coarse and fine timing data. The DLL divides a 2 ns interval into 64 distinct phases of 31.25 ps each, with 32 of these phases recorded by the TDC. Since the remaining 32 phases are complementary to the recorded ones, they can be reconstructed without additional storage, allowing the TDC to conserve 32 registers in its register bank. Additionally, it incorporates digital logic circuits for multi-echo measurement and can simultaneously collect TOF data and the number of SPAD pulse triggers.
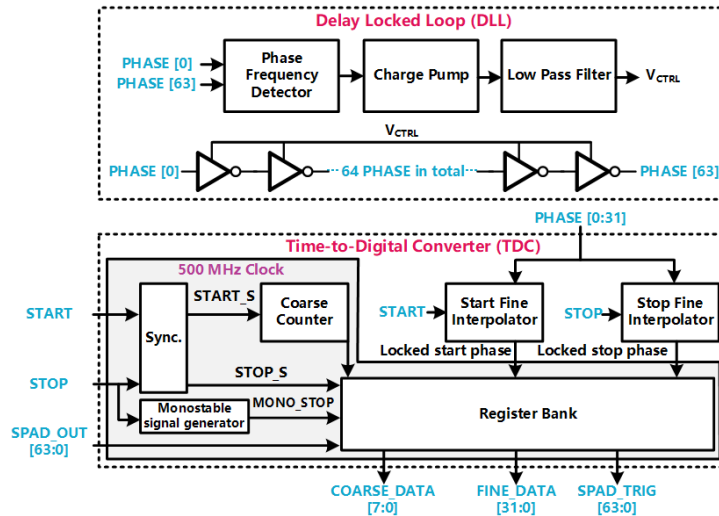

Figure B1   The block diagram of the DLL and TDC circuit.

The TDC comprises a synchronizer, a coarse counter, a monostable signal generator, a start and stop fine interpolator,

and a register bank. The synchronizer ensures alignment between coarse and fine data to avoid timing mismatches. It evaluates the first latch bit to determine if fine timing occurs in the first or second half of the clock cycle; if in the first half, the next rising edge aligns coarse timing, while in the second half, the falling edge is used. This approach provides at least half a clock cycle for stabilization, effectively mitigating jitter-induced discrepancies. This technique is applied to the rising edge of the START signal and whenever the STOP signal needs to be recorded to avoid errors.

Signals START_S and STOP_S, derived from the START and STOP inputs, activate the coarse counter and trigger data recording in the register bank. The monostable signal generator produces a MONO_STOP pulse based on the STOP signal, which samples the STOP_OUT signal (as shown in Fig. C2). The start and stop fine interpolators, each containing 32 latches, quickly capture fine-phase data when the START and STOP signals arrive. The register bank subsequently stores COARSE_DATA, FINE_DATA, and SPAD_TRIG signals.

Specifically, at the rising edge of the START signal (T1 in Fig. B2), the start fine interpolator captures the 32-bit start phase. Upon the rising edge of START_S (T2 in Fig. B2), the coarse counter begins counting, and the register bank stores the start phase. At the falling edge of the START signal (T3), the start fine interpolator outputs 32'h FFFFFFFF until the next START pulse. Similarly, at the rising edge of the STOP signal (T4), the stop fine interpolator captures the 32-bit stop phase and MONO_STOP is activated. The SPAD_OUT signal also arrives at this time. At the rising edge of STOP_S (T5), the register bank captures both the stop phase and coarse count data. The MONO_STOP signal falls at T6, and the register bank records the SPAD_OUT number. Finally, at the STOP signal's falling edge (T7), the stop fine interpolator outputs 32'h FFFFFFFF until the next STOP pulse, and SPAD_OUT is reset. As described in the previous paragraph, the synchronizer prevents mismatches between fine timing and coarse timing during their synchronization to ensure timing accuracy.
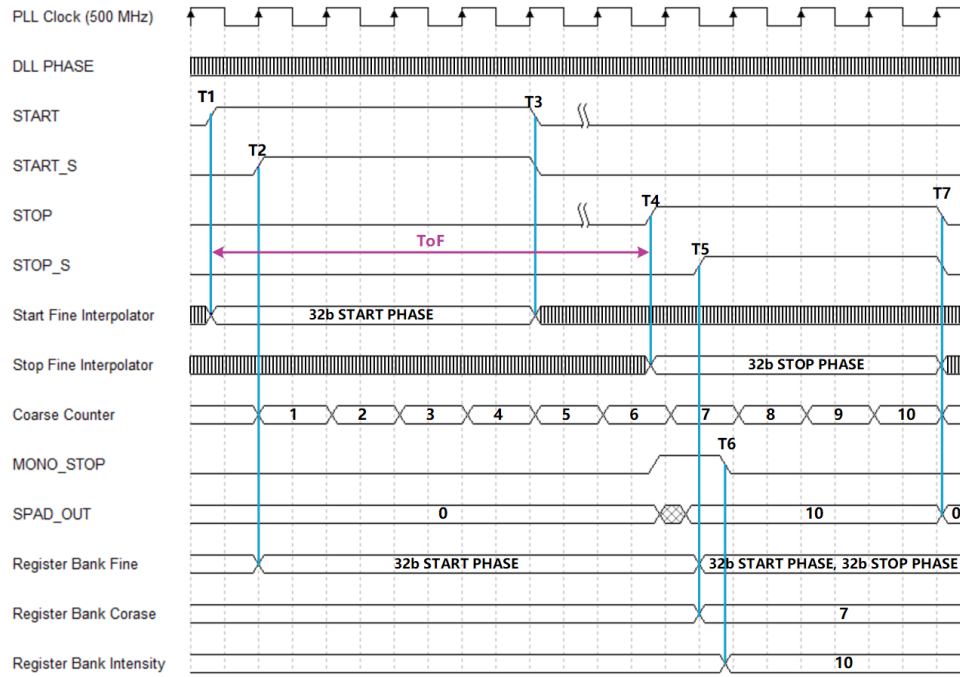

Figure B2   The signal timing diagram of the DLL and TDC circuit.

Notably, the proposed TDC is designed for multi-echo recording to capture potential effective TOF data without loss. For each echo, the register bank transfers recorded data to the next processing stage, and the synchronizer resets when the STOP signal goes low. This process introduces a 10 ns deadtime for the system. MONO_STOP is generated at the STOP signal's rising edge, with a 2 ns duration for stable sampling. At the MONO_STOP falling edge, SPAD_OUT [63:0] is locked into the register bank along with the TOF data.

Ambient light is a persistent source of interference, even when a narrow bandpass optical filter is applied to reduce irrelevant signals. Fortunately, ambient light interference, such as sunlight, does not coincide with laser pulse arrival, allowing the system to estimate whether a trigger is caused by a laser pulse based on the number of SPADs activated within a brief time interval. This count of triggered SPADs serves as an intensity indicator for the SPAD array, establishing the likelihood of coincident light triggers. After processing in the TDC, the decoder and subtractor module receives the COARSE_DATA and FINE_DATA, decodes and combines them, and outputs a final 14-bit TOF_DATA. Additionally, the module processes the 64-bit SPAD_TRIG data and condenses it into a 6-bit SPAD_TNUM value.

Appendix C   Histogram Module

To reduce the hardware cost associated with obtaining TOF peak values from a full histogram, this design adopts a partial histogram strategy implemented in three stages to identify the TOF peak more efficiently. Fig. C1 illustrates the block

diagram of the histogram module, which primarily consists of a counting and comparison module, registers, and a Finite State Machine (FSM) controller. At the end of each TDC time-of-flight measurement, the TDC sends the SPAD_TNUM and TOF_DATA directly to the histogram module for processing. As a result, there is no need for additional storage resources to record the raw time-of-flight data. The counting and comparison module is configured to process 5-bit input data, outputting the maximum frequency data (MF_DATA). To minimize hardware usage, the 14-bit TOF data (comprising 9-bit coarse and 5-bit fine values) is divided into two 5-bit segments and one 4-bit segment, which are processed sequentially to locate the TOF peak, known as the three- stage histogram strategy.
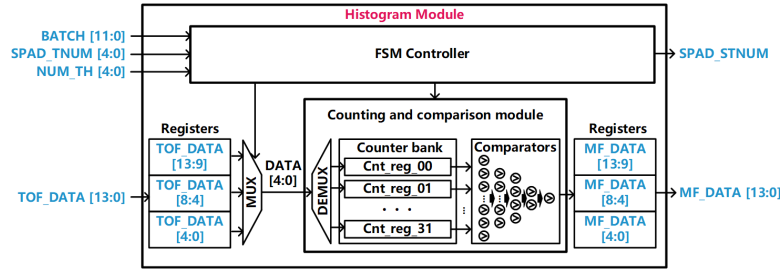

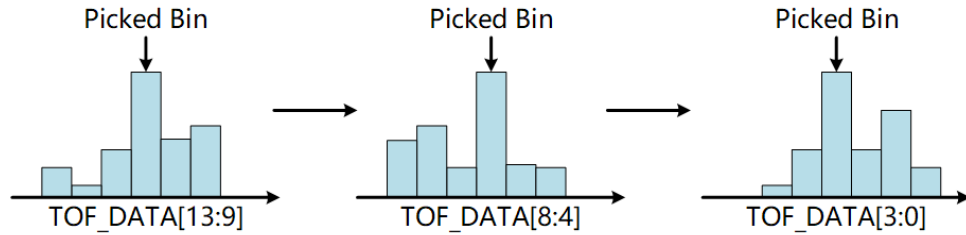**Figure C1**   The block diagram of the histogram module.

Figure C2   Illustration of partial histogram strategy.

The BATCH input signal controls the number of TOF data entries processed per histogram cycle, providing flexibility in output frequency configuration.

As shown in Fig. C2, the first configured BATCH count accumulates TOF_DATA[13:9] for histogram analysis. A comparator array then selects the peak BIN value, assigned as MF_DATA[13:9]. After each round, the registers are reset, and the next BATCH cycle begins. Only TOF data matching the MF_DATA[13:9] selection is processed in subsequent iterations to determine the TOF peak, reusing the counting and comparison module. The second stage processes MF_DATA[8:4], and the third stage processes MF_DATA[3:0]. The results from each stage are concatenated to form the complete MF_DATA[13:0], representing the final histogram calculation. This iterative peak detection and evaluation logic significantly reduces the required BIN depth and width, lowering both power consumption and hardware demands. Each BIN can store up to 128 pulse counts before overflowing. Therefore, the maximum number of pulses per measurement should not exceed 128 to avoid data overflow.

The three-stage histogram strategy works progressively, where the maximum frequency (MF_DATA) selected in each stage serves as the basis for the subsequent stage's selection. In the first stage, the algorithm calculates the frequency distribution of the high bits (TOF_DATA[13:9]) and selects the BIN value with the highest frequency as MF_DATA. In the second stage, this MF_DATA is used to narrow down the selection range for the middle bits (TOF_DATA[8:4]), and the most frequent value in this range becomes the new MF_DATA. In the third stage, the process is repeated for the lower bits (TOF_DATA[3:0]), with the MF_DATA from the second stage refining the selection. This progressive approach ensures that the most accurate TOF peak is selected by first filtering out less relevant data in each stage.

During execution, the SPAD_NUM associated with each TOF_DATA is also accumulated. Ultimately, the average SPAD_TNUM is calculated from the total TOF_DATA count, producing SPAD_STNUM. This value, alongside the histogram-derived peak distance, is used for subsequent walk error compensation. The histogram algorithm enables time-correlation detection based on the number of pulse triggers prior to TOF_DATA processing. To mitigate the influence of ambient light, an intensity threshold (NUM_TH) is set by reconfigurable registers before histogramming begins. As previously described, all intensity information is captured 2 ns after the first trigger, which aligns with the typical duration of a laser pulse. If a significant number of SPADs are triggered simultaneously, the event is likely a valid light trigger. Conversely, a lower trigger count may indicate interference from ambient sources.

Compared to the two-step histogram approach, the three-step histogram peak detection scheme proposed in this paper further minimizes the required storage space.If the two-step histogram method is used, the required RAM capacity is 8 bits * 128, while the three-step method only requires 5 bits * 128, resulting in a 37.5% reduction in RAM usage. The input histogram signals can be configured via registers, enabling hardware-based sunlight interference filtering, which enhances its suitability for single-point high-speed histogram measurements. Furthermore, the frame rate has been significantly

improved to meet the demands of high-speed 1D and 2D LiDAR measurements. Additionally, the proposed scheme stores signal intensity information, which can be utilized for subsequent reflectivity compensation.

It is worth noting that the hardware algorithm supports a maximum ranging speed of 10 kHz. However, due to the limited number of accumulated pulses, higher frame rates lead to reduced sunlight resistance and stability. As a result, the presented test results are based on a more practical frame rate of 1 kHz, balancing performance and reliability.

Appendix D   TEST result

The chip is fabricated in 180 nm BCD technology. The total size of the chip is 1.7 mm × 1.8 mm and the optic focal area is 0.6 mm × 0.6 mm, of which the active area is reconfigurable to be same as the optic focal point of laser echo by configuration registers. The breakdown voltage of the SPAD is around 20 V and the Dark Count Rate (DCR) of each SPAD is 1.4 kcps with the voltage of 5 V excess bias. At a wavelength of 905 nm, Photon Detection Probability (PDP) of 6% is achieved. To test the performance of the single point LiDAR system, the chip is made to a LiDAR module, as shown in Fig. D1.
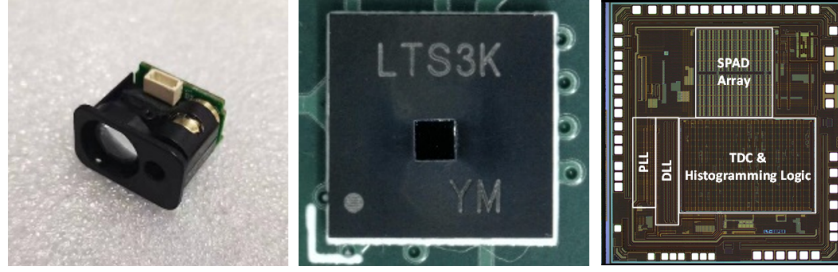

Figure D1   (a)The LiDAR module. (b) Packaged chip. (c) Die of the chip.

During module assembly, the reflected light is focused on the optical center of the SPAD array on the chip using a telecentric lens. After completing the module assembly, the laser is aligned with the target surface. By sequentially switching the SPAD_EN signals, the SPADs located at the optical echo center are identified, and those not in the optical center are disabled. After adjustment, only 25 out of 64 SPADs are triggered by the laser echo. Therefore, in the subsequent reflectivity compensation tests, the maximum number of triggers is limited to 25. The laser operates at a power of 5 W with a pulse width of 2 ns. The laser operates at a repetition frequency of 100 kHz, meaning that the histogram outputs a set of data after every 100 pulses. Due to the limitations of the transmitted and received optical power, the maximum measurable distance is approximately 15 m for white targets and 10 m for black targets, even though the TDC has a much greater range. To obtain more reliable distance measurements, the subsequent tests and comparisons are conducted at a distance of 10 m, which is within the measurable range for both black and white targets.

Appendix D.1   Sunlight Test

The test setup involved a 92 klux sunlight environment with a white wall target, as shown in Fig. D2(a). Fig. E1(b) presents the measurement fluctuations at a fixed distance of 10 meters, with an exposure repetition rate of 100 kHz, resulting in each data point representing an average of 100 measurements. Most of the data is centered around 10 meters, but due to sunlight interference, the actual output data shows deviations, resulting in fluctuations of up to 20 cm. However, no data loss or significant deviations are observed, demonstrating the effectiveness of the anti-interference capability.
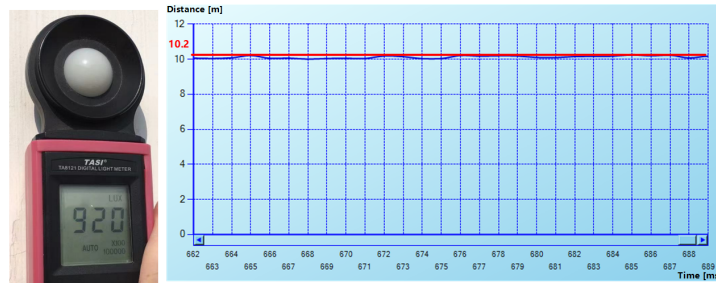

Figure D2   (a) 92 klux illumination and the wall as the target object. (b) Target ranging result graph.

$$\text{SNR} = 10\lg\left(\frac{\frac{\sum_{i=\text{real}-32\text{LSB}}^{i=\text{real}+31\text{LSB}}(N_{\text{bin}_i})^2}{64}}{\frac{\sum_{i=1}^{i=\text{BIN}_{\text{NUM}}}(N_{\text{bin}_i})^2 - \sum_{i=\text{real}-32\text{LSB}}^{i=\text{real}+31\text{LSB}}(N_{\text{bin}_i})^2}{\text{BIN}_{\text{NUM}}-64}}\right) \tag{D1}$$

To further validate the improvement in signal-to-noise ratio (SNR), the LiDAR module was tested with a substantial set of raw data under identical conditions. The SNR improvement was calculated as the ratio of the average square of TOF data counts within a 2 ns window (corresponding to the laser pulse duration in this design) to the average square of TOF data counts outside this interval.

As shown in the measured raw data in Fig. D3(a), recording only the first trigger under strong sunlight causes photon pile-up, obscuring the actual TOF peak and resulting in erroneous peak detection—indicating a closer distance that does not correspond to the object's true position. However, as depicted in Fig. D3(b), when all triggers are recorded, the true TOF peak can be identified through further data processing. Fig. D3(c) demonstrates that filtering out raw TOF data with intensities below 3 effectively enhances the signal quality.
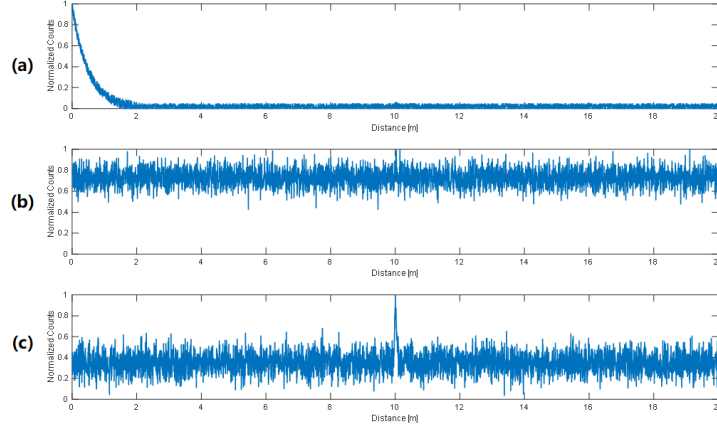

Figure D3   (a) The measured raw data, (b) recorded all triggers and (c) the filtered raw TOF data with normalized counts of y-axis.

The SNR values for the three cases are -11.36 dB, 0.22 dB, and 3.03 dB, respectively, resulting in an SNR improvement of 14.39 dB. These results clearly show that multi-echo recording combined with photon coincidence detection provides a significant improvement in SNR.

Appendix E   Linearity Characterization & Reflectivity Calibration

The DNL is ± 33ps and the INL is + 45.631/-92.302 ps. The TDC achieves a high LSB resolution of 31.25 ps. In this test, data is output through the histogram module at a rate of 1,000 frames per second. Fig. E1(a) illustrates the initial peak distance measurements obtained with different target reflectivities. As noted in the introduction, the use of macro-pixels introduces nonlinear errors due to reflectance variability. In reflectivity calibration, objects with higher reflectance produce stronger return signals, which in turn activate more SPADs in the array. This increased SPAD activation results in a reduction of propagation delay through the OR gate due to the cumulative effect of multiple triggers. By leveraging this characteristic, the number of activated SPADs is recorded, which is then used to estimate the object's reflectivity intensity. The recorded data is processed in the off-chip MCU, where reflectivity compensation is applied to ensure the accuracy and consistency of Time-of-Flight (TOF) measurements across objects with varying reflectivity levels.
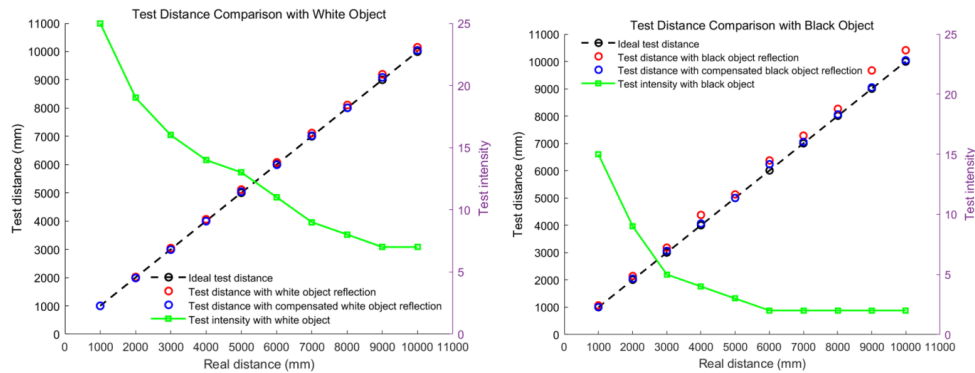

Figure E1   Ideal test distance, actual test distance, compensated test distance and intensity of (a) white object and (b) black object.

To further explain the compensation process: the average number of SPAD triggers for each object is inversely correlated with the distance, as higher reflectance surfaces cause more SPADs to trigger, which in turn results in more precise time

measurements. In the calibration process, the recorded number of SPAD triggers is used as a proxy for the reflectivity intensity. When analyzing actual test data, it was found that measurement error at various distances correlates primarily with the average number of SPAD triggers per signal echo. For example, a white reflective surface at a distance of 4 meters typically triggers an average of 14 SPADs, leading to an error of approximately 62 cm. In contrast, a black reflective surface at 1 meter generates an average of 15 SPAD triggers, with a corresponding error of about 68 cm.

This observed relationship indicates that the reflectivity compensation is heavily reliant on the exposure intensity—essentially, the number of SPAD triggers in relation to the reflectivity of the surface. The reflectivity compensation mechanism ensures that TOF measurements are corrected and consistent, regardless of the varying reflectivity levels of the objects being measured. Based on data analysis, Figure E3 provides the compensation curve, which shows the compensation distance values corresponding to the average number of SPAD triggers, which effectively reduces the error to within 3%.
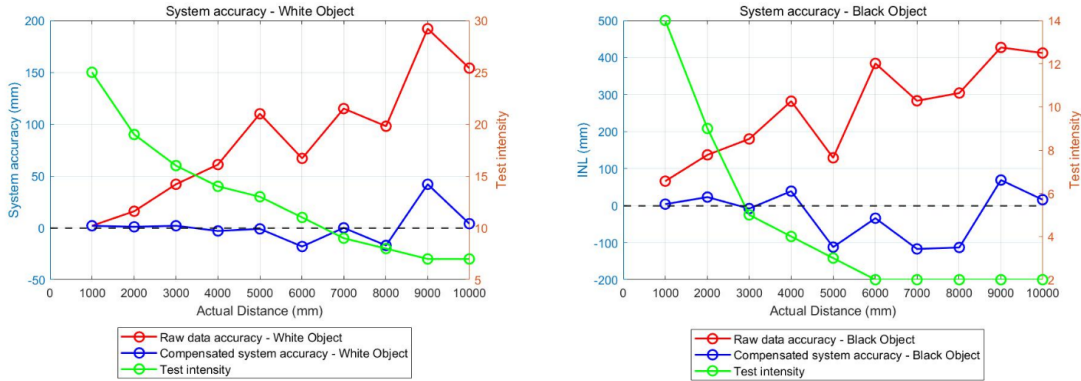

Figure E2   The actual distance of (a) white object and (b) black object.

Figure E2 illustrates the reflectivity error results for white and black objects before and after compensation. For the white object, the maximum deviation in system accuracy is 192 mm before compensation, which reduces to only 42 mm after compensation. Similarly, for the black object, the maximum error decreases from 400 mm before compensation to 105 mm after compensation. Within a 10-meter range, through reflectivity compensation, high-precision measurements with an accuracy of $\pm 2\%$ can be achieved for targets with any reflectivity. Additionally, the overall measured distance values align more closely with the actual curve, significantly reducing the nonlinearity of measurement errors. Reflectance compensation is essential in practical applications; however, it has received limited attention in existing SPAD-based systems. To the best of our knowledge, this paper is the first to propose a linear compensation method for reflectance based on pulse trigger counts.
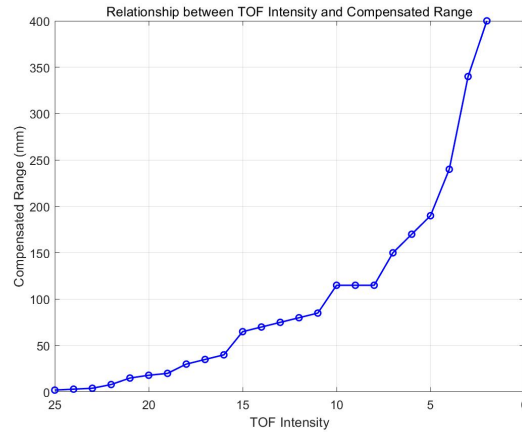

Figure E3   Compensated Range Versus ToF Intensity.